AIChE

Characterization of Taylor Vortex Flow in a Short Liquid Column

Rensheng Deng
Institute of Bioengineering and Nanotechnology, Singapore 138669, Singapore

Davis Yohanes Arifin, Ye Chyn Mak, and Chi-Hwa Wang
Dept. of Chemical and Biomolecular Engineering, National University of Singapore, Singapore 117576, Singapore

DOI 10.1002/aic.11919
Published online September 25, 2009 in Wiley InterScience (www.interscience.wiley.com).

We present a study on Taylor vortex flow in the annulus between a rotating inner cylinder and a stationary outer cylinder, featured with a wide gap (radius ratio is 0.613) and a short column (aspect ratio is 5.17). A particle image velocimetry (PIV) system was used to determine the position, shape, and velocity distribution of the vortices, by which the flow was also confirmed to lie in the nonwavy Taylor vortex regime for all operating conditions explored in this study. Our results suggest that end boundary effects are important, in which the vortex number decreases with decreasing column length. For a system with an aspect ratio of 5.17, six vortices appear in the gap with their position, size, and shape varying at different Reynolds numbers. The fluid velocities show an asymmetric feature with respect to the vortex centers, while the maximum axial and radial velocities increase almost linearly with the increasing reduced Reynolds number ($Re - Re_c$). In addition, computational fluid dynamics study was employed under the same conditions, and its results agree well with the PIV measurements. Overall, this study provides a quantitative understanding of the formation of Taylor vortices in a constrained space.
AIChE J, 55: 3056–3065, 2009
Keywords: computational fluid dynamics, fluid mechanics, transport, complex fluids, mathematical modeling

Introduction

Taylor vortex flow is a classical topic in fluid mechanics and it has found increasing application in processes such as reaction, filtration, and extraction. Usually, Taylor vortices are studied in devices that have narrow gap widths ($d/R \ll 1$, where $d = R_o - R_i$, and R_o and R_i are the radii of the outer and inner cylinders, respectively) and high aspect ratios ($\Gamma = H/d$, where H is the length of the liquid column) in an effort to minimize the effects of column ends on the formation of vortex patterns. However, it is also known that Taylor vortices forming in short, wide gap devices exhibit novel features. These include, for example, a much higher critical Reynolds number (Re_c) for transition from Taylor vortex flow to wavy vortex flow than in the case of infinitely long cylinders,[1,2] and the appearance of "anomalous" vortices in sudden start experiments.[3–5] Therefore, a short and wide liquid column will imply that small changes in boundary conditions may have significant influences on the pattern formation inside the gap.

Particle image velocimetry (PIV) has been widely used in recent years; however, only limited measurements of nonwavy Taylor vortex flow were reported, especially for a system with low Γ. Wereley and Lueptow[6] studied both nonwavy and wavy vortices ($\Gamma = 47.7$), although their major efforts were devoted to the latter. Painter and Behringer[7]

Correspondence concerning this article should be addressed to C.-H. Wang at chewch@nus.edu.sg.

examined the effects of spatial disorder on the transition to Taylor vortex flow ($\Gamma = 33.4$). Wereley et al.[8] measured the velocities in the rotating filtration of a suspension ($\Gamma =$ 45 to 48) using both PIV and particle tracking velocimetry. In a study of liquid flow between a rotating inner cylinder having a periodically varying radius in the axial direction and a stationary outer cylinder with a constant radius, Drozdov et al.[9] measured the axial and radial velocities with the help of PIV ($\Gamma > 20$). To our best knowledge, the only PIV study on a liquid column with $\Gamma < 10$ is that of Smieszek and Egbers,[10] while no quantitative velocity data were reported.

On the other hand, significant improvements in computational capacity and algorithms (such as finite element method) allow the application of computational fluid dynamics (CFD) simulations to the study of complex flows. For example, the commercial CFD software package, FLUENT, was employed by researchers to investigate single-phase[11–15] and two-phase Taylor–Couette flow systems.[16–18] The simulation results for both laminar and turbulent flows were reported to be satisfactory, although again a specific investigation on the short-column problem has not yet been available.

In this article, we present a study on Taylor vortex flow in a short liquid column within a wide annular gap. Both PIV measurements and CFD calculations were used to characterize the flow field in the presence of boundary effects.

Methodology

Experimental apparatus and procedure

A schematic diagram of the experimental apparatus is shown in Figure 1, which is similar to the system used by Deng et al.[19] A Newtonian mineral oil (with a density ρ of 0.86 g/cm^3 and a viscosity μ of 0.0297 Pa s) was used as the working fluid between a rotating inner cylinder ($R_i =$ 18.4 mm, $H = 60$ mm) and a stationary outer cylinder (R_o $= 30$ mm, $L = 200$ mm). This gives a gap width d of 11.6 mm, a radius ratio $\eta = R_i/R_o$ of 0.613, and an aspect ratio Γ of 5.17. The inner cylinder was made of stainless steel and was driven from the top. The rotation speed Ω of the motor could be changed continuously from 0 to 800 rpm (revolutions per minute) via a computer and the high viscosity of the mineral oil ensures a laminar liquid flow in the full speed range. The outer cylinder was made of Plexiglas. The entire apparatus was immersed in a Plexiglas square box filled with the same mineral oil in order to eliminate the optical distortion resulted from the difference in refractive indices of the mineral oil (1.476 at 20°C) and air. Note that, in addition, the outer cylinder must be thin (1 mm in our study) to minimize optical distortion. The transparency of both the outer cylinder and the square box makes it possible to illuminate the flow field with laser light and to photograph tracer particles in the annulus. The two cylinders were carefully adjusted to make sure that both were perfectly vertical and concentric. Unless otherwise specified, the distance between the bottoms of the inner and outer cylinders (H_B) was always set at 72 mm, and the distance between the top of the inner cylinder and the liquid surface (H_T) was set at zero. The Re of the flow

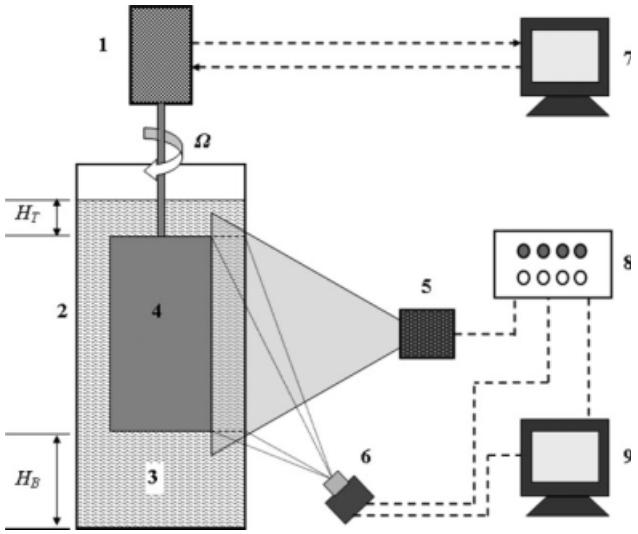

Figure 1. Schematic diagram of the experimental setup.

(1) Motor, (2) outer cylinder, (3) working liquid, (4) inner cylinder, (5) laser generator, (6) camera, (7) computer for motor control, (8) synchronizer, and (9) computer for PIV system.

$$Re = \Omega R_i d\rho/\mu \tag{1}$$

is less than 519.

A PowerView 2D PIV system from TSI Company (Shoreview, Minnesota, USA) was used to monitor the liquid flow, by which the position, shape, and velocity distribution of Taylor vortices could be determined. The laser light sheet was generated by a Laser Pulse™ Solo Mini Dual Nd:YAG laser and was introduced from the sidewall to illuminate the liquid plane of interest. The laser sheet was adjusted to be perpendicular to one side of the square box and through the common axis of the two cylinders, so that a radial plane of the annulus was illuminated. Silver-coated hollow glass spheres with an average diameter of 16 μm and a density of 1.6 g/cm^3 were added as tracer particles. Images of the tracer particles were captured by a PowerView™ 4M 2K $\times$ 2K camera placed perpendicular to the laser light sheet. Two photos were taken within a short time interval (dT ranges from 200 to 2000 μs) and the image data were then sent to the computer for processing. A Laser Pulse Computer-Controlled Synchronizer was used to coordinate the operation of the whole PIV system. The image data were analyzed by the Insight™ Parallel Processing Ultra PIV software using a cross-correlation algorithm to generate the velocity vectors in the illuminated plane.

Before the PIV measurements were carried out, a calibration step was performed in order to convert the unit of displacement from pixel to millimeter. This was done by utilizing a snapshot of an object of known size to calibrate the pixel distance. As the time scale was obtained directly from the synchronizer, the actual velocity could then be determined.

It is well known that hysteresis effects may play an important role in Taylor vortex formation. Unlike the usual "sudden start" and "quasi-steady" schemes, the inner cylinder in our experiments was run at the maximum rotational speed of

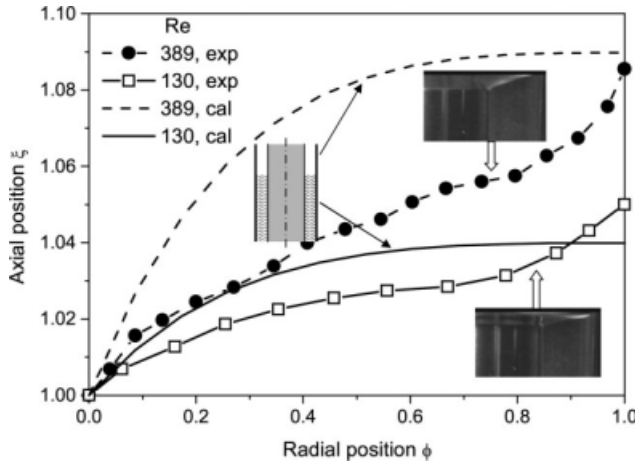

Figure 2. Shape of the top surface.

The dashed and solid curves show the results calculated from Eqs. 4 and 5 based on a half-infinitely long column model. The curves with symbols show the heights obtained from the two photos taken from a high-speed video camera.

800.4 rpm for 1 min, followed by suddenly decelerating to the desired rotational speed. This is to ensure uniform dispersal of the tracer particles in the liquid. After examining the velocity fields obtained at different moments after the "sudden deceleration," a waiting time of 12 min was selected to wait for the flow to reach the final steady state before the velocity measurements were conducted. The repeated tests showed that the above method could generate reproducible steady state velocity data.

In this study, only the liquid column in the annular gap is of interest, and the plane on the right-hand side (denoted by the rectangular window bounded by the dashed lines in Figure 1) is always chosen to show the vortex structure in the context. The center of the bottom surface of the inner cylinder is set as the origin of the coordinate system, with the positive abscissa r pointing to the right along the radial direction and the positive coordinate z pointing upwards. Two dimensionless coordinates are defined as

$$\Phi = (r - R_i)/d \tag{2}$$

and

$$\xi = z/H. \tag{3}$$

Thus, the bottom-left corner of the PIV window has a coordinate of $(\Phi, \xi) = (0, 0)$ and the up-right corner of (1, 1).

Numerical method

The commercial CFD software, FLUENT 6.1, was used to simulate the Taylor vortex flow. The fluid domain was constructed and meshed by the software package Gambit 2.1, with the same dimensions as those used in experiments. Triangular mesh elements were used for those zones adjacent to the curved-shape top surface, while quadrilateral mesh elements were used elsewhere. The mesh size was not uniform, for example, a grid density of 10 points/mm in both axial and radial directions was adopted for the annular gap where the vortex pattern forms, while an average of 5 points/mm was used for the liquid layer below the gap. The dependence of calculated results on grid size was checked and it was found that a further increase in grid density did not improve the accuracy of calculated vortex shape and velocity distribution.

The mesh was then introduced into the software package Fluent for simulating the Taylor vortex flow. The flow was assumed to be axisymmetric, which is valid in the nonwavy Taylor flow regime. All walls were treated as no-slip, except for the top surface which is assumed to be a zero shear stress boundary. The simulation followed the same "sudden deceleration" procedure as adopted in the experiments, in an effort to model any hysteresis effects that might be present. Given the initial guesses for pressure and velocity, the continuity and momentum equations were numerically solved by a finite volume method to generate the pressure and velocity fields. To obtain better convergence, the relaxation factors were gradually increased from an initial value of 0.1 to a final value of 0.6 as iterations progress.

One problem to be solved is the determination of the shape of top surface. Because the fluid rotates, the centrifugal force results in an uneven surface. If Taylor vortex flow is absent and the liquid column is half-infinitely long, as shown in Figure 2, it is possible to predict the surface shape

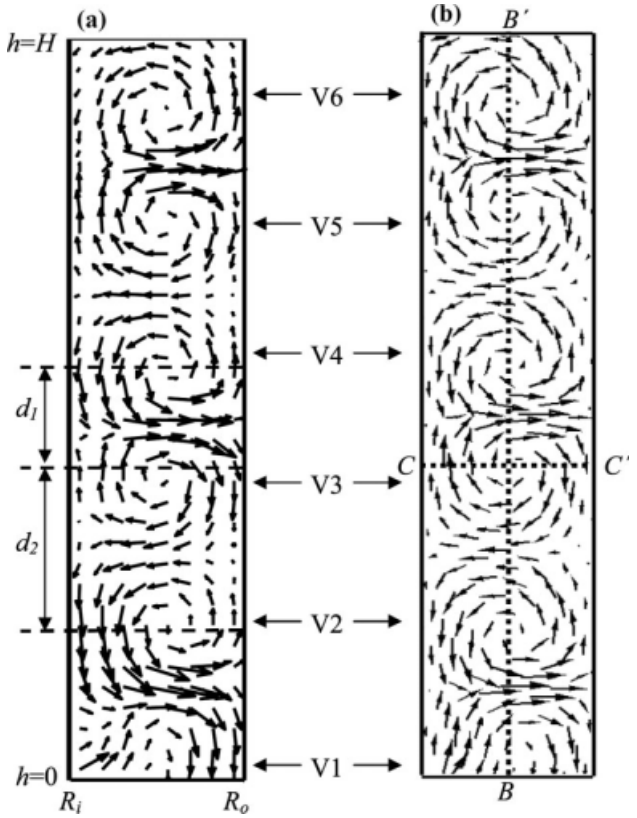

Figure 3. Typical vortex structure from (a) PIV measurements and (b) CFD simulation.

Re = 194. The lines BB' and CC' cross the vortex centers vertically and horizontally, respectively. d_1 and d_2 denote the distances between two adjacent vortex centers.

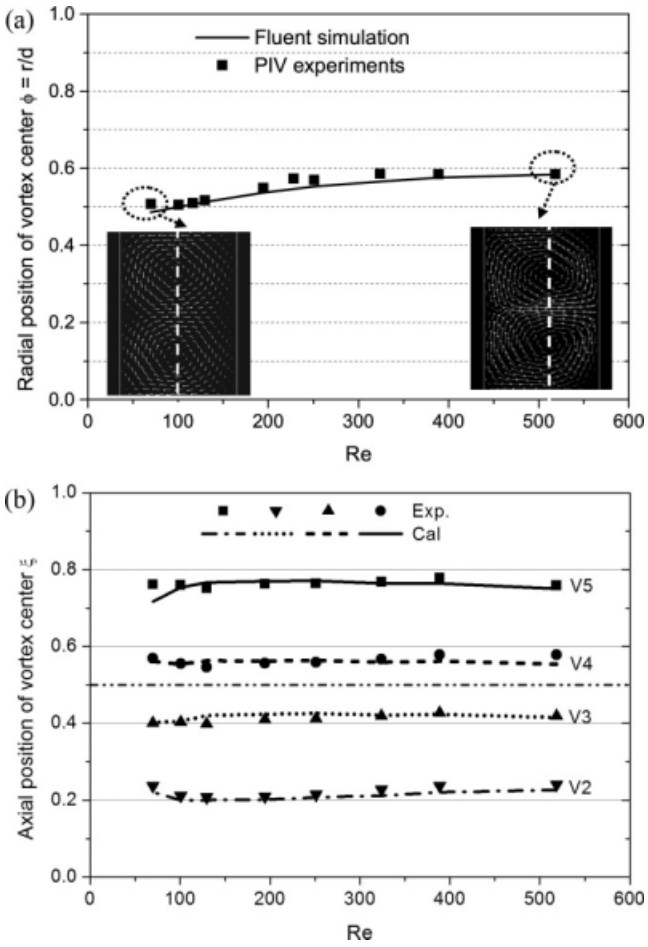

Figure 4. (a) Radial and (b) axial positions of Taylor vortex centers at various *Re*.

The inserted pictures in (a) are the velocity vector plots obtained from simulation for $Re = 70$ (left) and 519 (right), in which the dashed lines cross the vortex centers vertically.

by using, for example, the procedure as proposed by Kaye.[20] Here the interfacial tension between gas, liquid, and walls is ignored. For a Newtonian fluid, the shape of the surface calculated by Kaye[20] can be expressed as

$$h(r) = h_0 + \left(\frac{1}{2}A^2r^2 - \frac{1}{2}A^2R_i^2 + 2AB\ \ln(r/R_i) - \frac{1}{2}B^2r^{-2} + \frac{1}{2}B^2R_i^{-2}\right)/g, \quad (4)$$

where

$$A = \frac{\Omega R_i^2}{R_i^2 - R_o^2}, \quad B = \frac{\Omega R_i^2 R_o^2}{R_o^2 - R_i^2}. \quad (5)$$

Here h_0 is the height at $r = R_i$. In the case of $R_i = 18.4$ mm and $R_o = 30$ mm, the surface shapes for $Re = 130$ and 389 are shown in Figure 3. Note that here the surface height is nondimensionalized by the column height. It can be seen that the surface height increases with increasing radial position and rotation speed. The height difference across the gap can be significant at high rotation speeds, for example, it is almost half of the gap width at the Re of 389.

However, the liquid column in this study is short rather than infinity, and the formation of Taylor vortex further complicates the flow in the system. As a result, it is difficult to directly predict the surface shape. Instead, we can measure the surface shape directly from the images taken by a high-speed video camera and use it in simulation, as shown in Figure 2. The surface height differences across the gap (calculated by subtracting the ξ value at the inner cylinder wall from that at the outer cylinder wall) are about 0.045 and 0.08 for Re of 130 and 389, respectively, close to the values (0.04 and 0.09, respectively) predicted by the aforementioned simple model. However, a significant difference between the two can be observed: the model predicts a logarithmic-type curve gradually approaching a constant at the outer cylinder, whereas the experimental measurement shows a more continuous increase in surface height. This may result from the interfacial tension that helps the mineral oil to easily spread on the surface of the outer cylinder made of Plexiglas.

Results and Discussion

Taylor vortex structure

From both experiments and simulation we observe the transition from a pure circulating flow around the inner cylinder to a stable Taylor vortex flow at a Re_c of 62 and the data show no sign of wavy vortices up to at least a Re of 519 in the present system. Yim et al.[21] studied the onset of Taylor vortex for various values of radius ratio with the aspect ratios of 33 and 72. According to their results, a system composed of a rotating inner cylinder and a stationary outer cylinder with a radius ratio of 0.613 has a critical Taylor number of 2500, corresponding to a Re_c of 62.9 for our case, which is close to our measured value of 62.

On the other hand, Edwards et al.[2] reported the onset of wavy vortex for Taylor–Couette flow with a finite length. Their results show that the decrease in aspect ratio (Γ) results in the increase in transition Re to wavy vortex flow. For example, with a radius ratio of 0.87, the transition occurs at $Re_w = 134.7$ for $\Gamma = 34.129$ and $Re_w > 1500$ for both $\Gamma = 4.015$ and $\Gamma = 6.022$. Thus, Re_w may be larger

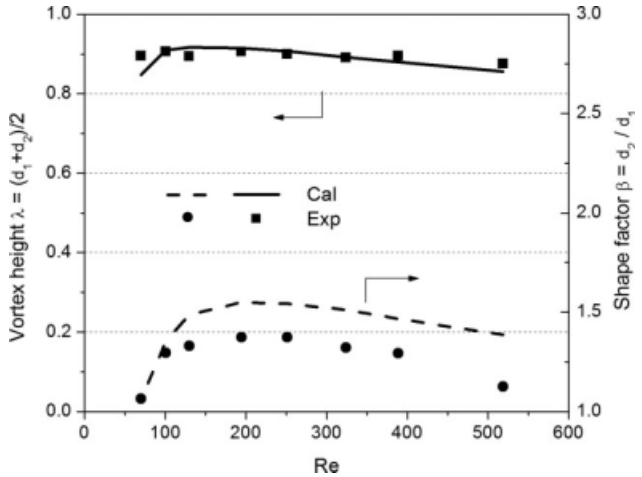

Figure 5. Average vortex size and deformation factor at various *Re*.

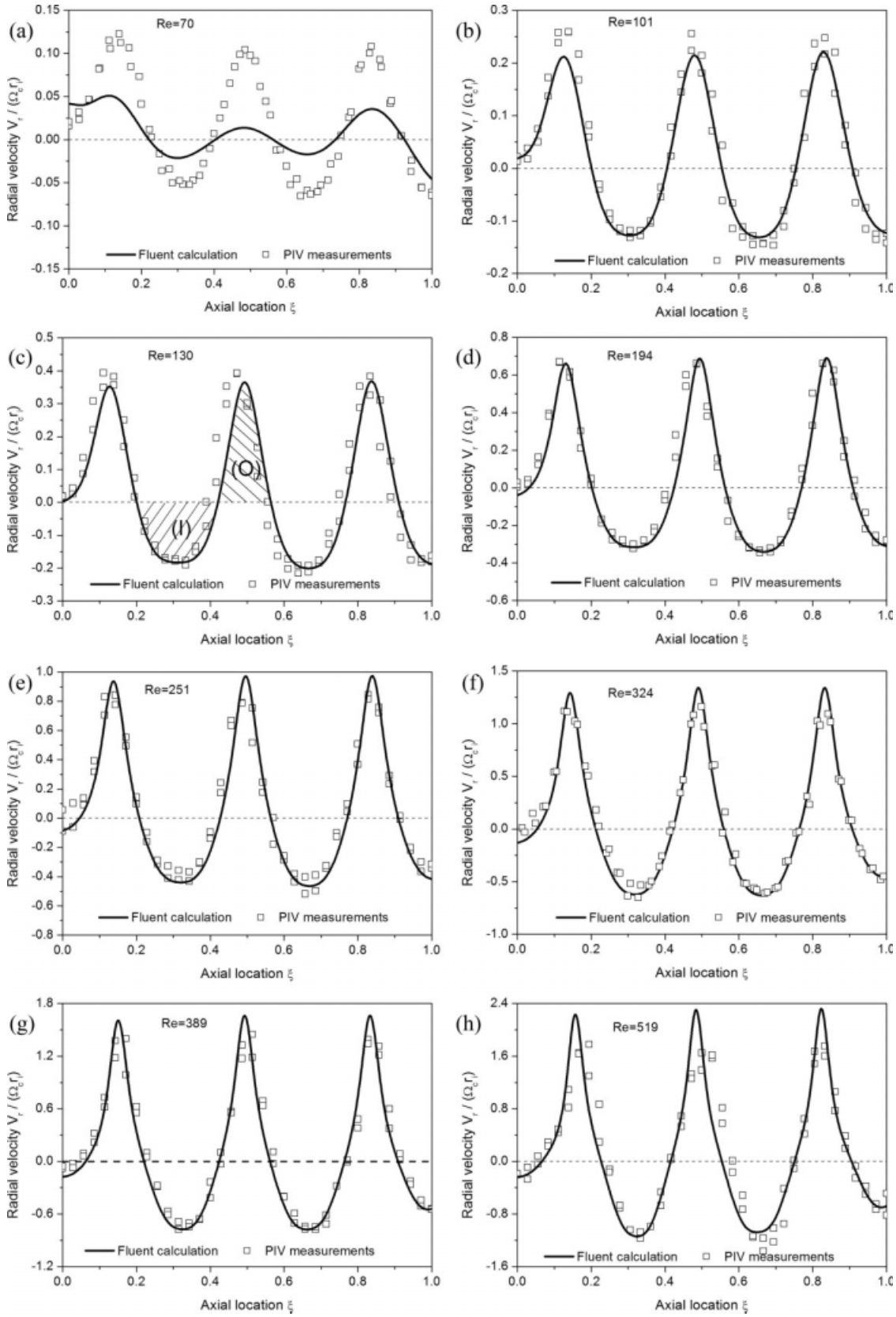

Figure 6. Radial velocity along line BB' in Figure 3b at (a) *Re* = 70, (b) *Re* =101, (c) *Re* = 130, (d) *Re* = 194, (e) *Re* = 251, (f) *Re* = 324, (g) *Re* = 389, (h) *Re* = 519.

than 1500 in our system with a Γ value of 5.17, already beyond the maximum Re of 519 used in this study. This is quite different from the observations on systems with a large aspect ratio. For instance, Andereck et al.[22] presented a phase diagram on flow patterns in between two concentric cylinders. Corresponding to a stationary outer cylinder, the transition from one-dimensional flow to Taylor vortex occurs at $Re_c = 120$ and to wavy vortex at $Re_w = 140$ in a water system with a radius ratio of 0.883 and an aspect ratio from 20 to 48 (typically 30). Wereley and Lueptow[6] reported the Re_c of 102 at the onset to Taylor vortex and 131 at the onset to wavy vortex corresponding to $\Gamma = 47.7$. Thus, it can be seen that the short-column apparatus corresponds to a much wider range of Re for nonwavy Taylor vortex flow than those with a high aspect ratio. The occurrence of the first transition to nonwavy vortex flow at a lower rotational speed and the subsequent transition to wavy vortex flow at a higher rotational speed is possibly due to the end-wall vortices related to the Ekman layers which alter the vortical structure.[1]

Figure 3a shows a typical chart of velocity vectors obtained from our PIV measurements. Six vortices appear in the annulus along the vertical direction, namely V1 to V6 from bottom to top. Only half of the vortex V1 is seen in the observation window and the other half lies in the liquid layer below the inner cylinder. The distance between the centers of V4 and V3 is denoted as d_1 and that between V3 and V2 is d_2. From the velocity vectors we can see that d_1 and d_2 correspond to outflow and inflow regions, respectively.

According to Czarny et al.,[23] if end-walls are fixed to the stationary outer cylinder as in this study, the imbalanced pressure gradient and centrifugal forces can result in an inflow at the end-walls, and this Ekman layer flow determines the rotation of the vortices nearest the end-walls. Thus, vortex V1 always rotates clockwise in our experiments as shown in Figure 3, and the rotation of other vortices is subsequently determined.

Figure 3b shows the calculated velocity field from FLUENT simulations. It can be seen that the simulation results agree qualitatively with the experimental data and exhibit all of the experimental features. Quantitative comparisons will be discussed in the following sections.

Vortex position and shape

To characterize the vortex positions, we define the vortex center as the location where the fluid velocity equals to zero in the gap (excluding the wall boundaries where zero velocity is observed as a result of the no-slip boundary conditions there). Because of the limitation in resolutions of PIV methods and numerical simulation, a spline interpolation was needed to find out the axial and radial coordinates corresponding to zero velocity. Here the radial position of vortex centers is based on the average of V3 and V4 only.

As shown in Figure 4a, when the Re is below 100, the radial position of the vortex centers locate in the middle of the liquid gap, corresponding to $\Phi = 0.5$. With the increasing Re, the vortex centers tend to shift toward the outer cylinder wall. The velocity vector plots inserted in Figure 4a show that V3 and V4 are quite symmetric about the vortex center at $Re = 69$, whereas they deform significantly at $Re = 519$. The observation that vortex centers are displaced toward the outer cylinder in Taylor vortex flow regime agrees with the observation of Smieszek and Egbers.[10]

Figure 4b shows the axial positions of vortices V2, V3, V4, and V5 at various Re. It can be seen that the vortices are not equally distributed along the column height. To know the vortex shape clearly, the above data are replotted in Figure 5 by defining vortex height λ and shape factor β as the following:

$$\lambda = (d_1 + d_2)/2d, \tag{6}$$

$$\beta = d_2/d_1. \tag{7}$$

It can be seen that λ and β measure the average height of vortices in the gap and the relative height of two adjacent vortices, respectively.

As we can see from Figure 5, λ is nearly constant. In this study, λ is about 0.9, which means the vortex is rather "fat" with an average vortex height always less than the gap width. On the other hand, β increases from about 1.0 at the Re_c to a maximum of about 1.5 at $Re = 194$, followed by a gradual decrease with further increasing Re. The fact that β is larger than 1 for all Re in this study means the height of inflow region is always longer than that of outflow region. The measured value of β is equal to 1.33 at $Re = 124$, which agrees well with the value of 1.3 reported by Wereley and Lueptow[6] for the same Re.

In-plane velocity distribution

Figure 6 shows the radial velocity profiles along the line BB' shown in Figure 3b, from both PIV measurements and CFD simulation at various Re. The line BB' vertically crosses the vortex centers, and thus the axial velocity is always zero along this line. It can be seen that the radial velocity shows a periodic feature. However, the velocity distribution is not symmetrical along the line BB'. The shape of the velocity peak in the outflow regime (with a positive radial velocity) is sharper than the inflow regime (with a negative radial velocity), and the maximum outflow velocity is higher than the absolute value of maximum inflow velocity.

As shown in Figure 6, the magnitude of radial velocity increases with increasing Re. The calculated velocity in general agrees well with the measurements except for the deviations observed at very low and high Re. For example, the measured velocity is significantly higher than the calculated value when $Re = 70$. The deviation possibly results from the inaccuracy in determining the distance traveled by tracer particles during the time interval dT. Since this Re is just above the Re_c, the in-plane axial and radial velocities are very small compared with the azimuthal velocity. Thus, although the particles may travel by just a short distance because of the in-plane velocity, they can be carried much farther by the azimuthal velocity and a higher-than-true velocity is measured. For a high Re such as 519, however, the measured maximum radial velocity is lower than the CFD prediction. This may be attributed to the limitation of PIV resolution which will be discussed later.

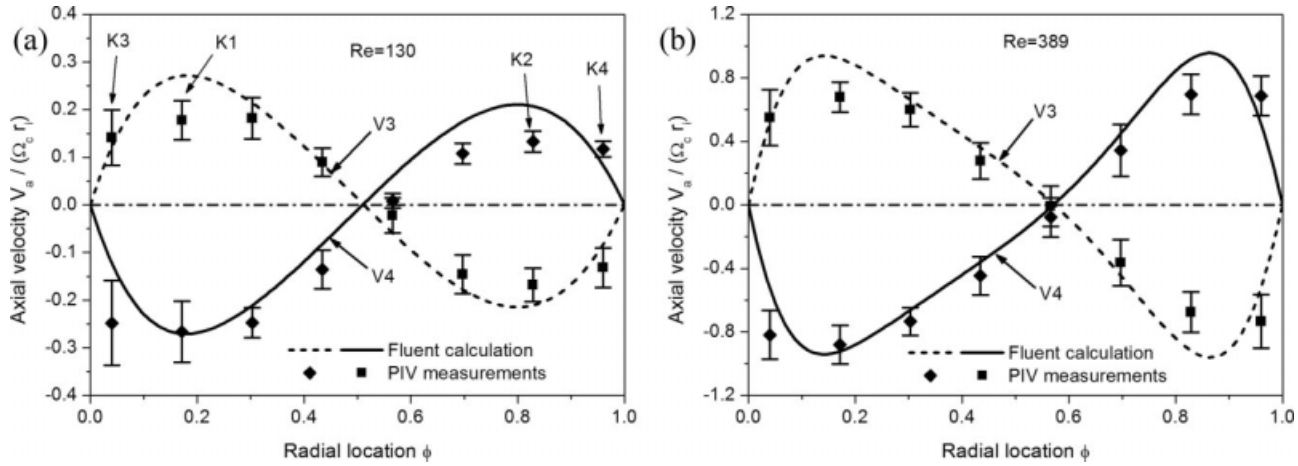

Figure 7. Axial velocity profile along line CC' in Figure 3b at (a) *Re* =130 and (b) *Re* = 389.

Figure 7 shows the axial velocity profile along the line CC′ in Figure 3b. Here CC′ is perpendicular to the cylinders and across the center of V3 or V4, thus the corresponding radial velocity along this line is zero. The two curves for vortices V3 and V4 with the same *Re* are almost symmetric about the line corresponding to zero velocity. A comparison between Figures 7a, b shows that the radial location of the zero velocity point shifts to high ξ values with increasing *Re*, which is in correspondence to the shift of vortex center in Figure 4a. Each velocity curve has a maximum (flowing upwards) and a minimum (flowing downwards). Taking those curves of V3 as an example, it can be seen that the maximum is larger than the absolute value of the minimum at $Re = 130$, while they are almost equal at $Re = 389$.

In simulation, the velocities at both the inner and outer cylinder walls reach zero as a result of the no-slip boundary conditions adopted. However, the measured axial velocities of those points near the walls in Figure 7, for example, K3 and K4, are still quite some distance from zero. On the other hand, points located in regimes of highest velocity, for example, K1 and K2, have lower axial velocities than predicted. The deviation comes from the limited resolution of PIV method.

In the PIV measurement, the flow field is divided into small interrogation windows, in which the positions of those tracer particles are tracked to generate the velocity representing the interrogation window via a cross-correlation method. As shown in Figure 8a, the radial velocity measured from window W1 is smaller than the true velocity at point M1 because of the leveling-off effects by the low velocities surrounding M1. On the contrary, the axial velocity at point M2, which should be close to zero because of the no-slip conditions at the wall, will be measured as a negative velocity from window W2 because of the inclusion of downward velocity vectors in the window. The problem can be partially solved by zooming in the field of interest and generating more vectors in a certain area, which requires a corresponding increase in the number density of tracer particles to satisfy the necessity of sufficient tracer particles in each interrogation window. However, a high concentration of tracer particles may significantly alter the physical properties of the system, for example, increasing the viscosity of the working fluid.

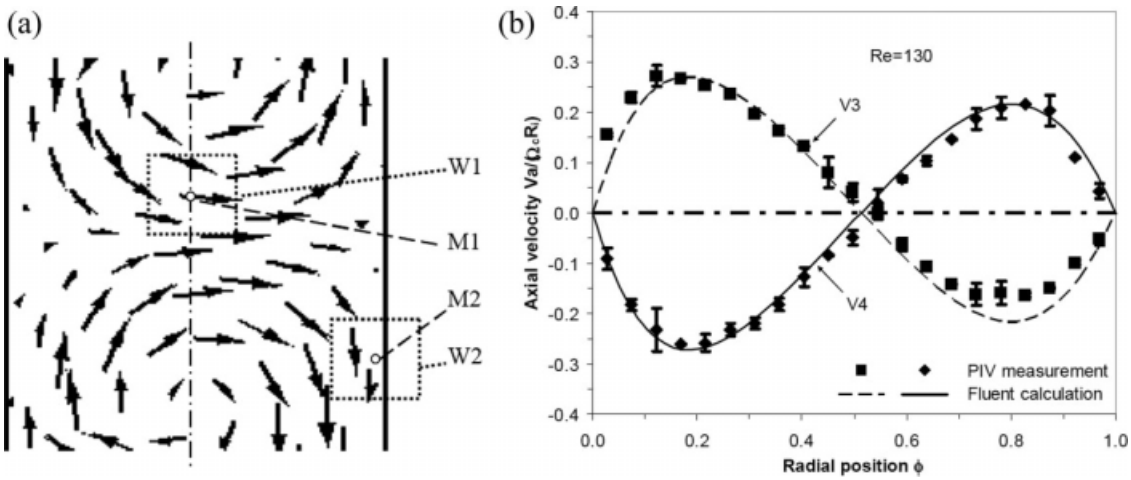

Figure 8. (a) A schematic diagram to show the possible error that resulted from the insufficient resolutions of the PIV system. (b) Axial velocity along the vortex center measured by another PIV system.

In (a), W1 and W3 represent the interrogation windows to generate velocity vectors at M1 and M2, respectively. In (b), $Re = 130$.

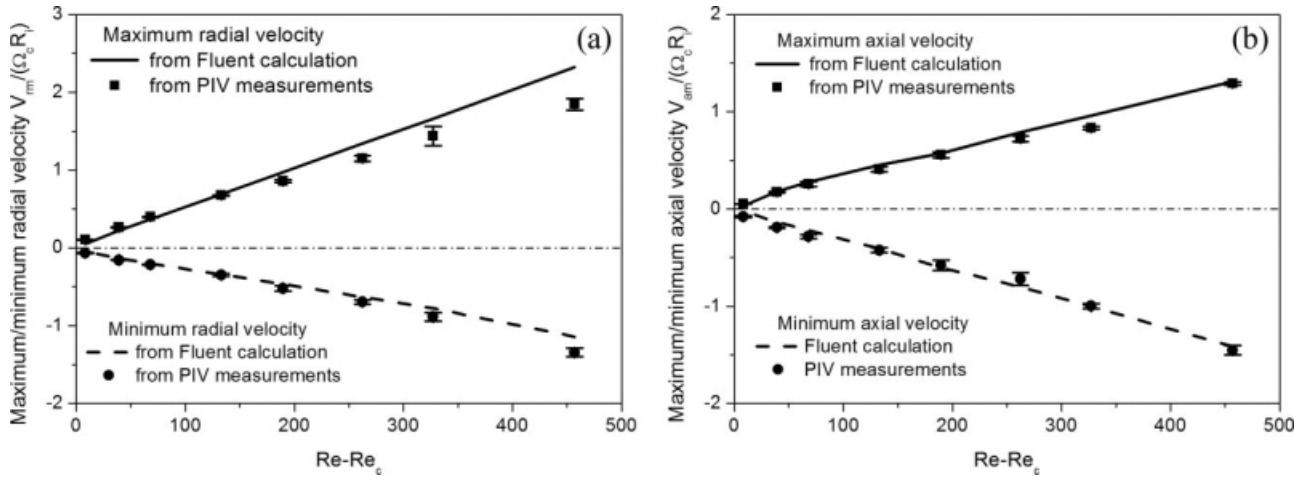

Figure 9. Plots of (a) maximum and minimum radial velocity vs. reduced *Re* and (b) maximum and minimum axial velocity vs. reduced *Re*.

To overcome this issue, another PIV camera with improved resolution and different type of tracer particles was used. The tracer particles are made of silicon carbide with a diameter of 2 μm and a density of 3.2 g/cm^3, whose images in the fluid flow are then taken by a FlowSense 4M (2047 $\times$ 2047 pixels) CCD camera from Dantec Dynamics (Bristol, UK). Because of their smaller size, we were able to include more tracer particles in each interrogation window and the resolution of the velocity vectors was improved. Figure 8b shows the axial velocity profiles measured by the new PIV system at $Re = 130$. It clearly shows that the measured axial velocity now tends to decrease to zero at the wall, and the quantification accuracy is improved.

The improved accuracy by the new PIV system can also be verified by checking the flow rate. For example, if we integrate the radial velocity along the axial location in Figure 6c, the area of shadow (I) should be equal to that of shadow (O) because of the balance of inward and outward fluxes for the steady Taylor vortex flow. The average inward/outward flow rate for one vortex is calculated as half of the product of the area aforementioned and $2\pi R_c$ (R_c is the radius corresponding to vortex centers), which is 2.46 E -5 m^3/s. On the other hand, the flow rate for vortex V3 or V4 can be obtained from CFD simulations, which is 2.16 E -5 m^3/s for $Re = 130$. The inward/outward flow rate is about 1.15 times of the azimuthal flow rate in a single vortex. Compared with the Couette flow, the occurrence of such a significant inward/outward flow can enhance the exchange between the inner and outer liquid layers, which is important for the development of a novel extractor.[16] From the curve of $Re = 130$ in Figure 8, the flow rate of upward/downward flows can be determined as 2.46 E -5 m^3/s, which balances the inward/outward flow rate well.

Maximum/minimum axial and radial velocities

Figure 9 shows the calculated and measured maximum/minimum axial and radial velocities at different *Re*. Here the maximum (minimum) axial velocity is obtained by comparing the peak values in Figures 6 and 8 and choosing the maximum (minimum). As shown in Figure 9a, the maximum/minimum radial velocity almost linearly increases/decreases with the increasing reduced *Re* ($Re - Re_c$), suggesting that the intensity of Taylor vortex flow depends on the *Re* of the primary flow (circulating around the inner cylinder). The absolute value of the slope for the maximum velocity curve is about 2.1 times of that for the minimum velocity.

Figure 9b shows the maximum/minimum axial velocity. Similarly, the maximum/minimum velocity increases/decreases linearly with the increasing reduced *Re*. Here the maximum and minimum axial velocity curves are symmetrical about the zero axial velocity line. In the range of our operating conditions, the maxima of axial and radial velocities are found to be always less than 20% of the azimuthal velocity of the inner cylinder, again confirming that the Taylor vortex flow is weaker than the primary flow.

The almost linear relationship between the maximum radial velocity and *Re* agrees with the theoretical analysis provided by Czarny et al.[24] Moreover, the relationship can explain the profile of maximum bubble size that can be captured in a Taylor vortex at various *Re*.[19] However, this is different from Davey's nonlinear correlation between axial (or radial) velocity and reduced *Re* in an infinitely long liquid column.[25] Two reasons may be attributed to such a difference: (1) Davey's expansion is most applicable very near the transition to Taylor vortex flow and (2) the velocity field in the short column as in this study is significantly influenced by the Ekman vortices. Note that although the absolute deviation at low *Re* is low, the relative deviation is quite significant, as shown in Figure 6a.

Vortex structure at even lower column heights

Now we consider an annulus partially filled with the working fluid to an even lower height h. As shown in Figure 10a, the experimental results show that the vortex number increases with the increasing height, from 3 for a half filled gap to finally 6 for a fully filled gap. This resulted from the fact that a longer liquid column provides more space for

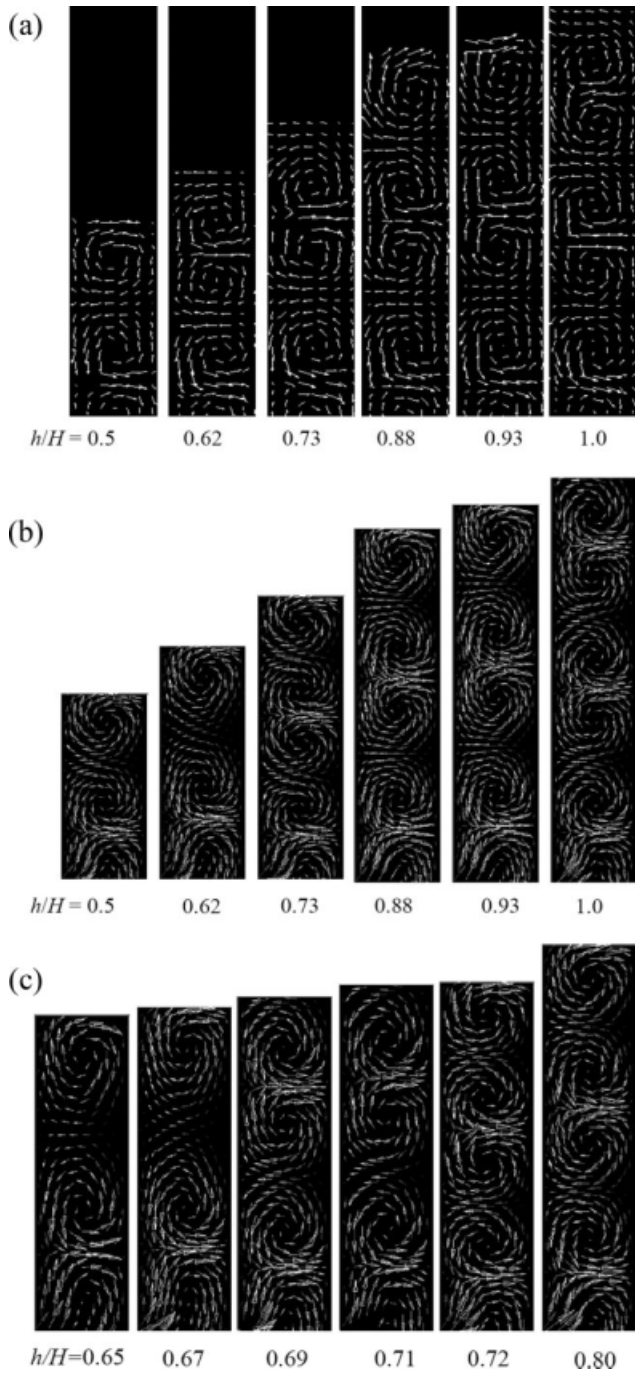

Figure 10. The Taylor vortex structures (a) from PIV measurements and (b) from CFD simulation in the gap partially filled with the working fluid to various heights *h/H*. (c) The vortex structures calculated for several *h/H* values between 0.65 and 0.8. *Re*=130.

Taylor vortices to form and stay in the gap. As stated earlier, vortex V1 always rotates clockwise in our experiments, and the rotation direction of the top vortex (which is near the free surface) can be either clockwise or anticlockwise depending on the number of vortices in the gap is odd or even. The simulation results shown in Figure 10b agree with the experimental observations except that the calculated vortex number increases from 3 to 5 between $h/H = 0.62$ and 0.73, different from the critical heights seen from experiments.

Because the vortex number must be an integer, one can expect a stepwise jump rather than a continuous change in vortex number. It will be interesting to understand the transition when vortex number escalates distinctly from N to $N + 1$. For this purpose, simulations were conducted on the vortex flow with the liquid layer height increasing from 0.65 to 0.8. The results are shown in Figure 10c.

When h/H increases from 0.62 to 0.65, there are still three vortices in the gap. However, the vortices V1 and V2 shift upwards with the increasing liquid height, but to a less extent than V3 does. As a result, the distance between V2 and V3 keeps increasing. When h/H reaches 0.69, a new vortex, V4, appears on the top of the annulus, which rotates anticlockwise, opposite to the previous top vortex V3. Meanwhile, vortices V1, V2, and V3 move downwards to accommodate for the newcomer. However, the four-vortex structure does not persist for long. A further increase of the liquid height to $h/H = 0.72$ results in the formation of a new vortex V5 on the channel top, which returns to a clockwise rotation again. Next, the distance between V2 and V3 and the distance between V4 and V5 increase continuously until sufficient space is accumulated for the occurrence of V6 at $h/H > 0.93$. These observations suggest that the appearance of vortex structures is very sensitive to the liquid height change in a certain range (for example, $0.65 < h/H < 0.72$) due possibly to the existence of a free top surface. And this might be the reason for the disagreements in vortex number between experimental observation and simulation prediction ($h/H = 0.62$ and 0.73).

Conclusions

Using PIV technique, we have quantitatively characterized the Taylor vortex flow in a short liquid column contained inside a wide annular gap. Because of the existence of strong end effects, the system exhibits several new features. Nonwavy Taylor vortex flow persists for *Re* from 62 up to at least 519, a range much wider than that in a long column. At high *Re*, the vortices deviate from the centerline of the gap and show an asymmetric shape. Both the maximum axial and radial velocities in the vortices show a linear correlation with the reduced *Re*. On the other hand, the vortex number in the gap is very sensitive to the column height. For example, it gradually increases from 3 for a half-filled column to 6 for a full-filled column, although the major change happens in a narrow height range. The calculation results from FLUENT simulation in general agree well with the experimental observations. This study can provide a quantitative understanding of the Taylor vortex structure in such a constrained system.

Acknowledgments

This project was supported by the Science and Engineering Research Council (SERC), the Agency for Science Technology and Research (A*STAR), Singapore, and the National University of Singapore under the grant R279-000-208-305.

Literature Cited

1. Cole JA. Taylor-vortex instability and annulus-length effects. *J Fluid Mech*. 1976;75:1–15.
2. Edwards WS, Beane SR, Varma S. Onset of wavy vortices in the finite-length Couette-Taylor problem. *Phys Fluids A*. 1991;3:1510–1518.
3. Benjamin TB. Bifurcation phenomena in steady flows of a viscous fluid. I. Theory. *Proc R Soc Lond Ser A*. 1978;359:1–26.
4. Koga JK, Koschmieder EL. Taylor vortices in short fluid columns. *Phys Fluids A*. 1989;1:1475–1478.
5. Bielek CA, Koschmieder EL. Taylor vortices in short fluid columns with large aspect ratio. *Phys Fluids A*. 1990;2:1557–1563.
6. Wereley ST, Lueptow RM. Spatio-temporal character of non-wavy and wavy Taylor-Couette flow. *J Fluid Mech*. 1998;364:59–80.
7. Painter BD, Behringer RP. Effects of spatial disorder on the transition to Taylor vortex flow. *Europhys Lett*. 1998;44:599–605.
8. Wereley ST, Akonur A, Lueptow RM. Particle-fluid velocities and fouling in rotating filtration of a suspension. *J Membr Sci*. 2002; 209:469–484.
9. Drozdov S, Rafique M, Skali-Lami S. An asymmetrical periodic vertical structures and appearance of the self induced pressure gradient in the modified Taylor flow. *Theor Comput Fluid Dyn*. 2004;18: 137–150.
10. Smieszek M, Egbers C. Flow structures and stability in Newtonian and non-Newtonian Taylor-Couette flow. *J Phys Conf Ser*. 2005; 14:72–77.
11. Marchisio DL, Barresi AA, Fox RO. Simulation of turbulent precipitation in a semi-batch Taylor-Couette reactor using CFD. *AIChE J*. 2001;47:664–676.
12. Marchisio DL, Barresi AA. CFD simulation of mixing and reaction: the relevance of the micro-mixing model. *Chem Eng Sci*. 2003; 58:3579–3587.
13. Dutta PK, Ray AK. Experimental investigation of Taylor vortex photocatalytic reactor for water purification. *Chem Eng Sci*. 2004; 59:5249–5259.
14. Wang L, Marchisio DL, Vigil RD, Fox RO. CFD simulation of aggregation and breakage processes in laminar Taylor-Couette flow. *J Colloid Interface Sci*. 2005;282:380–396.
15. Wang L, Vigil RD, Fox RO. CFD simulation of shear-induced aggregation and breakage in turbulent Taylor-Couette flow. *J Colloid Interface Sci*. 2005;285:167–178.
16. Baier G, Graham MD. Two-fluid Taylor-Couette flow with countercurrent axial flow: linear theory for immiscible liquids between corotating cylinders. *Phys Fluids*. 2000;12:294–303.
17. Baier G, Graham MD, Lightfoot EN. Mass transport in a novel two-fluid Taylor vortex exactor. *AIChE J*. 2000;46:2395–2407.
18. Zhu X, Vigil RD. Banded liquid-liquid Taylor-Couette-Poiseuille flow. *AIChE J*. 2001;47:1932–1940.
19. Deng R, Wang CH, Smith KA. Bubble behavior in a Taylor vortex. *Phys Rev E*. 2006;73:036306.
20. Kaye A. The shape of a liquid surface between rotating concentric cylinders. *Rheol Acta*. 1973;12:206–211.
21. Yim SSS, Lo MYA, Titchener-Hooker N, Ayazi Shamlou P. The dependence of residence time distribution on flow in co-axial cylinder devices. *Bioprocess Eng*. 1998;19:221–227.
22. Andereck CD, Liu SS, Swinney HL. Flow regimes in a circular Couette system with independently rotating cylinders. *J Fluid Mech*. 1986;164:155–183.
23. Czarny O, Serre E, Bontoux P, Lueptow RM. Spiral and wavy vortex flows in short counter-rotating Taylor-Couette cells. *Theor Comput Fluid Dyn*. 2002;16:5–15.
24. Czarny O, Serre E, Bontoux P, Lueptow RM. Interaction between Ekman pumping and the centrifugal instability in Taylor-Couette flow. *Phys Fluids*. 2003;15:467–477.
25. Davey A. The growth of Taylor vortices in flow between rotating cylinders. *J Fluid Mech*. 1962;14:336–368.

Manuscript received Dec. 21, 2008, and revision received Mar. 16, 2009.